

Dark matter admixed neutron star properties in the light of X-ray pulse profile observations

ZHIQIANG MIAO,¹ YAOFENG ZHU,¹ ANG LI,¹ AND FENG HUANG¹

¹*Department of Astronomy, Xiamen University, Xiamen, Fujian 361005, China; liang@xmu.edu.cn; fenghuang@xmu.edu.cn*

ABSTRACT

The distribution of the dark matter (DM) in DM-admixed-neutron stars (DANSs) is supposed to be either a dense dark core or an extended dark halo, which is subject to the DM fraction of DANS (f_χ) and the DM properties, such as the mass (m_χ) and the strength of the self-interaction (y). In this paper, we perform an in-depth analysis of the formation criterion for dark core/dark halo and point out that the relative distribution of these two components is essentially determined by the ratio of the central enthalpy of the DM component to that of the baryonic matter component inside DANSs. For the critical case where the radii of DM and baryonic matter are the same, we further derive an analytical formula to describe the dependence of f_χ^{crit} on m_χ and y for given DANS mass. The relative distribution of the two components in DANSs can lead to different observational effects. We here focus on the modification of the pulsar pulse profile due to the extra light-bending effect in the case of a dark-halo existence and conduct the first investigation of the dark-halo effects on the pulse profile. We find that the peak flux deviation is strongly dependent on the ratio of the halo mass to the radius of the DM component. Lastly, we perform Bayesian parameter estimation on the DM particle properties based on the recent X-ray observations of PSR J0030+0451 and PSR J0740+6620 by the Neutron Star Interior Composition Explorer.

Keywords: Dark matter (353); Neutron stars (1108); Pulsars (1306)

1. INTRODUCTION

Neutron stars (NSs) could act as astrophysical laboratories to test the possible effects of dark matter (DM) and indirectly measure DM particle properties (Goldman & Nussinov 1989). Multimessenger observations have been explored to constrain the structure of the DM-admixed NSs (DANSs), which in turn puts limits on DM parameter space. In this context, there are many studies on how DM may impact various observable properties of NSs, such as the mass-radius relation (Narain et al. 2006; Sandin & Ciarcelluti 2009; Ciarcelluti & Sandin 2011; Leung et al. 2011; Li et al. 2012a,b; Leung et al. 2012; Goldman et al. 2013; Xi-ang et al. 2014; Kouvaris & Nielsen 2015; Li et al. 2015; Rezaei 2017; Mukhopadhyay et al. 2017; Panotopoulos & Lopes 2017; Motta et al. 2018; Wang et al. 2019), the surface temperature (Bertone & Fairbairn 2008; Kouvaris 2008; Gonzalez & Reisenegger 2010; de Lavallaz & Fairbairn 2010; Kouvaris & Tinyakov 2010; Fan et al. 2011), the kinematics and rotation properties (Pérez-García & Silk 2012), the tidal deformability (Ellis et al. 2018; Nelson et al. 2019; Das et al. 2019; Fasano et al. 2020; Das et al. 2020; Quddus et al. 2020; Das et al. 2021; Husain & Thomas 2021; Lee et al. 2021; Sagun

et al. 2021; Sen & Guha 2021; Dengler et al. 2022; Di Giovanni et al. 2022; Rafiei Karkevandi et al. 2022), or the gravitational wave waveform during the postmerger stage (Kopp et al. 2018; Bezares et al. 2019; Bauswein et al. 2020).

In general, DM can form either a dense core inside the NS or an extended halo surrounding the NS, which would result in different or even opposite effects on some properties of DANSs. Since the detection of the GW170817 binary NS merger (Abbott et al. 2017), the DANS study through the tidal deformability has gained much attention. For example, it is found that an extended dark halo could dramatically enhance the stellar tidal deformability Λ (Nelson et al. 2019), while a dense dark core will affect it in an opposite way (Ellis et al. 2018; Sagun et al. 2021). The upper bound of tidal deformability for a NS with $1.4 M_\odot$ $\Lambda_{1.4} \leq 800$ (Abbott et al. 2017) reported by the LIGO/Virgo collaboration has been used to provide new constraints on the DM properties (Ellis et al. 2018; Quddus et al. 2020; Husain & Thomas 2021; Sagun et al. 2021). It is suggested that future detection of large tidal deformability, which exceeds the expected range of NS, could be interpreted as a dark halo (Nelson et al. 2019). The possibility of the $2.6 M_\odot$ compact object in the binary merger GW190814 (Ab-

bott et al. 2020) being a DANS has also been investigated in the literature (Das et al. 2021; Lee et al. 2021; Wystub et al. 2021).

The formation of a dark halo or dark core should be determined by the nature of DM and the amount of DM accumulated in DANSs. As illustrated in e.g., Ivanytskyi et al. (2020); Rafiei Karkevandi et al. (2022), light DM particles tend to form a dark halo while heavy ones prefer to form a dark core. In the scenario of self-interacting DM, the strength of DM self-interaction also plays an important role here. Qualitatively, the larger the strength of the self-repulsive interaction, the easier it is for DM to occupy a larger volume; that is, the easier it is to form a dark halo. However, there is no general criterion in the current literature to determine whether it is a DM halo or a dark core when a specific DM model is assumed. This paper aims to perform an in-depth analysis of the formation criterion for dark core/dark halo. As deduced in later sections, we point out that the central enthalpy is the key factor. For example, if the central enthalpy of baryonic matter (h_B^c) is larger than that of DM (h_D^c), then there forms a dark core; otherwise, there should be a dark halo. For the critical case where the radii of DM and baryonic matter are the same, the amount of DM in DANS, represented by the DM fraction of DANS (f_χ) at a fixed DANS total mass (M_T), should depend on a specific DM model. We further derive an analytical formula to describe the dependence of f_χ^{crit} on the DM particle mass (m_χ) and the strength of DM self-interaction.

X-ray oscillations have been observed from a few millisecond pulsars. The shape of the pulsation in the X-ray flux (i.e. pulse profile) encodes information about the surface properties of the NS as well as its exterior spacetime. Therefore, when a dark halo formed in DANSs, pulses emitted from the surface of baryonic matter should suffer an additional gravitational potential and modification of the pulse profile is expected. Di Giovanni et al. (2022) firstly mentioned such kind of effect in their discussion, but so far, no detailed numerical calculations have been performed on how the dark halo would modify the pulse profile emitted from the surface of the baryon component. Such an analysis is carried out for the first time in the present work. As we will see later, this modification sensitively depends on the ratio of the halo mass to the radius of DM component M_{halo}/R_D . For compact dark halo with $M_{\text{halo}}/R_D \simeq 0.01$, the modification in pulse profile can reach about 10%. Therefore modified pulse-profile modeling is necessary when one applies the NICER measurements to study DANSs. As an example, we show how we

incorporate the recent NICER data for studying DANSs and constraining the dark DM particle properties.

This paper is organized as follows. In Section 2 we present the formalism of self-interacting fermionic DM. In Section 3 we study the structure of DANSs. In particular, we focus on deriving the criterion of the formation of core/halo and estimating the critical amount of DM. In Section 4 we discuss the effect of dark halos on the DANS pulse profiles. Then in Section 5 we perform bayesian parameter estimation on DM properties by using the NICER results from X-ray pulse-profile modeling. We summarize in Section 6.

2. DARK MATTER EQUATION OF STATE

In this work, we consider DM to be made of self-interacting fermions with masses from MeV to GeV. We assume that the DM particles are non-annihilating as in asymmetric DM (Zurek 2014). Neglecting finite temperature effects, the energy density of DM with particle mass m_χ is given by (Narain et al. 2006; Nelson et al. 2019):

$$\epsilon_\chi = \epsilon_{\text{kin}} + m_\chi n_\chi + \frac{(\hbar c)^3 n_\chi^2}{m_I^2}, \quad (1)$$

where n_χ is the DM number density and ϵ_{kin} is the DM kinetic energy. m_I represents the energy scale of the self-interaction via a Yukawa type in the repulsive case (see more discussions in Kouvaris & Nielsen 2015; Gresham & Zurek 2019), providing stabilization with respect to the gravitational collapse (Nelson et al. 2019; Ivanytskyi et al. 2020). For weak interaction, $m_I \sim 300$ GeV as mediated by W or Z bosons, while for strongly interacting DM particles, m_I is assumed to be ~ 100 MeV according to chiral perturbation theory (Narain et al. 2006).

The kinetic energy can be calculated by the model of an ideal Fermi gas:

$$\epsilon_{\text{kin}} = \frac{1}{\pi^2 (\hbar c)^3} \int_0^{k_F} dk k^2 (\sqrt{k^2 + m_\chi^2} - m_\chi), \quad (2)$$

where $k_F = \hbar c (3\pi^2 n_\chi)^{1/3}$ is the Fermi momentum. By denoting $x \equiv k_F/m_\chi$ and $y \equiv m_\chi/m_I$, the energy density and pressure are determined as:

$$\epsilon_\chi = \frac{m_\chi^4}{8\pi^2 (\hbar c)^3} \left[(2x^3 + x) \sqrt{1 + x^2} - \sinh^{-1}(x) \right] + \frac{m_\chi^4 y^2 x^6}{(3\pi^2)^2 (\hbar c)^3}, \quad (3)$$

$$P_\chi = \frac{m_\chi^4}{24\pi^2 (\hbar c)^3} \left[(2x^3 - 3x) \sqrt{1 + x^2} + 3 \sinh^{-1}(x) \right] + \frac{m_\chi^4 y^2 x^6}{(3\pi^2)^2 (\hbar c)^3}. \quad (4)$$

The DM equation of state (EOS), i.e., the pressure-density relation, is then obtained.

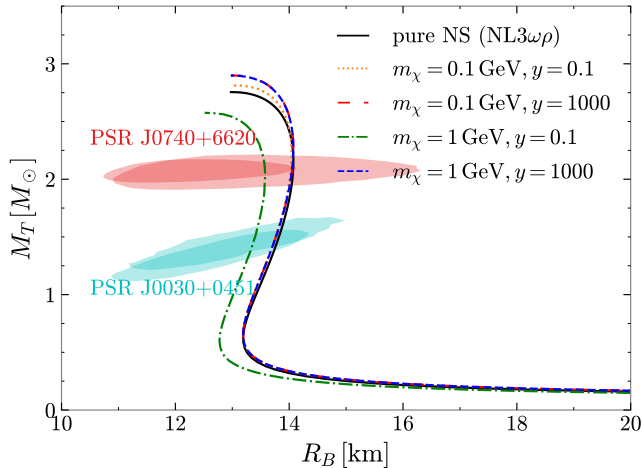


Figure 1. Total gravitational mass as a function of the radius of the baryon component. The black solid curve is for pure NSs from the NL3 $\omega\rho$ EOS (Horowitz & Piekarewicz 2001) without DM, whereas the other curves are for DANs with DM fraction $f_\chi = 0.05$ (Ellis et al. 2018). The NICER’s mass-radius measurements for PSR J0030+0451 (Miller et al. 2019; Riley et al. 2019) and PSR J0740+6620 (Riley et al. 2021; Miller et al. 2021) from X-ray pulse profile modeling are also shown in the shaded regions, respectively.

3. DARK MATTER ADMIXED NEUTRON STAR STRUCTURE

The DANs stable configuration in hydrostatic equilibrium is obtained by solving the two-fluid Tolman-Oppenheimer-Volkoff (TOV) equations (Kodama & Yamada 1972; Sandin & Ciarcelluti 2009; Ciarcelluti & Sandin 2011) for the pressure and the enclosed mass,

$$\frac{dP_B}{dr} = -\frac{GM(r)\epsilon_B(r)}{r^2} \times \left(1 + \frac{4\pi r^3 P(r)}{M(r)}\right) \left(1 + \frac{P_B(r)}{\epsilon_B(r)}\right) \left(1 - \frac{2GM(r)}{r}\right)^{-1} \quad (5)$$

$$\frac{dP_\chi}{dr} = -\frac{GM(r)\epsilon_\chi(r)}{r^2} \times \left(1 + \frac{4\pi r^3 P(r)}{M(r)}\right) \left(1 + \frac{P_\chi(r)}{\epsilon_\chi(r)}\right) \left(1 - \frac{2GM(r)}{r}\right)^{-1} \quad (6)$$

$$\frac{dM_B}{dr} = 4\pi r^2 \epsilon_B(r), \quad (7)$$

$$\frac{dM_D}{dr} = 4\pi r^2 \epsilon_\chi(r), \quad (8)$$

where $M(r) = M_B(r) + M_D(r)$ and $P(r) = P_B(r) + P_D(r)$ with the subscript index ‘B’ and ‘D’ stand for the baryonic matter and DM components respectively. Given the central pressures of the two components $P_{B,c}$ and $P_{\chi,c}$ as initial conditions, we solve Eqs. (5-8) by

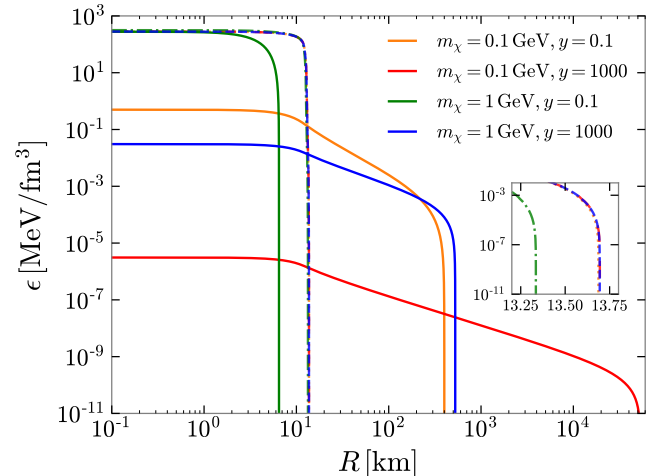


Figure 2. Energy density as a function of the stellar radius for $M_T = 1.4 M_\odot$ DANs. The DM fraction is fixed at $f_\chi = 0.05$ (Ellis et al. 2018). Solid curves show density profiles for the DM component, while dashed curves for the baryon component.

employing the Runge-Kutta 4th order method. In each iteration step we calculate the densities of the two components from their pressures using corresponding EOSs. We integrate Eqs. (5-8) outward until the pressures of the baryonic matter and DM vanish. This gives the radii of the baryon component R_B and the DM component R_D . The gravitational masses of two components are then $M_B(R_B)$ and $M_D(R_D)$, respectively. Hereafter, we denote $f_\chi = M_D(R_D)/M_T$ as the DM fraction, where $M_T = M_B(R_B) + M_D(R_D)$ is the total gravitational mass. For the description of the baryonic matter, we use the NL3 $\omega\rho$ EOS, developed in the relativistic effective field theories to fit nuclear matter saturation and properties of finite nuclei (Horowitz & Piekarewicz 2001). The DM EOS can be varied by changing the particle mass m_χ and the interaction strength y . Note that we have assumed the baryonic matter and DM components couple essentially only through gravity since the non-gravitational interactions between them could be negligibly small (Marrodán Undagoitia & Rauch 2016; Rrapaj & Reddy 2016).

3.1. Mass-radius relation

In Fig. 1 we show the mass-radius relation of DANs with DM fraction $f_\chi = 0.05$ (Ellis et al. 2018). The calculations are done for two cases of DM interaction strengths ($y = 0.1$ and 1000) and two cases of DM particle mass ($m_\chi = 0.1$ and 1 GeV). We see that in the case of small interaction strength ($y = 0.1$), the DM effects on mass-radius are dominated by the DM particle mass, namely light DM particles ($m_\chi = 0.1$ GeV)

tend to increase the maximum mass. In contrast, heavy DM particles ($m_\chi = 1 \text{ GeV}$) would instead reduce the maximum mass of NSs. In the case of large interaction strength ($y = 1000$), regardless of the DM particle mass, one observes an increase in the total gravitation mass but nearly unchanged radii for the baryon components.

The density profiles of $M_T = 1.4 M_\odot$ DANs are further reported in Fig. 2, for both cases of DM interaction strengths and particle masses. The DM fraction is again fixed at $f_\chi = 0.05$. The influences of the DM properties on the mass-radius relations of DANs observed above in Fig. 1 can then be understood as follows:

1) In the case of small interaction strength ($y = 0.1$), light DM particles ($m_\chi = 0.1 \text{ GeV}$) would form a dark halo, i.e., $R_D > R_B$. Therefore most DM gathers into the halo, thereby leaving only a small mass fraction inside the DANs to impose a negligible influence on the stellar structure. As a result, one observes an increase in the total gravitation mass, which comes from the halo mass, but nearly unchanged radii for the baryon components. The situation changes for heavy DM particles with $m_\chi = 1 \text{ GeV}$, as they form a dense core in the NS interior. Under this circumstance, the gravitational effect of the core cannot be neglected, and consequently, the radius of the baryon component shrinks.

2) In the case of large interaction strength ($y = 1000$), the repulsion could force DM to form a halo structure. In this case, we would again expect an increase in the total mass and an unchanged radius for the baryon component. As a result, the mass-radius relation could be indistinguishable for different DM particle masses. Nevertheless, it is possible to probe the m_χ value from the radius of DM component R_D , for example, through the measurements of tidal deformability Λ (Abbott et al. 2017), as it approximately scales with the fifth power of the stellar radius, i.e., $\Lambda \propto R_D^5$.

3.2. Dark core and dark halo

As noted earlier, the distributions of DM in DANs present two scenarios, namely dark halos ($R_D > R_B$) and dark cores ($R_D < R_B$). The formation of a dark core/halo depends not only on the DM properties but also on the DM amount. The actual amount of DM accumulated in NSs should depend on the evolutionary history and the external environment of the NSs. See, e.g., Kain (2021) for detailed discussions on the mixing of DM with ordinary matter in NSs. However, a thorough exploration of the accumulation mechanisms is still lacking and would be an interesting topic to explore in the future. For the present purpose, we take two representative values of the DM fraction, $f_\chi = 0.05$ (Ellis et al. 2018) and $f_\chi = 10^{-4}$ (Nelson et al. 2019).

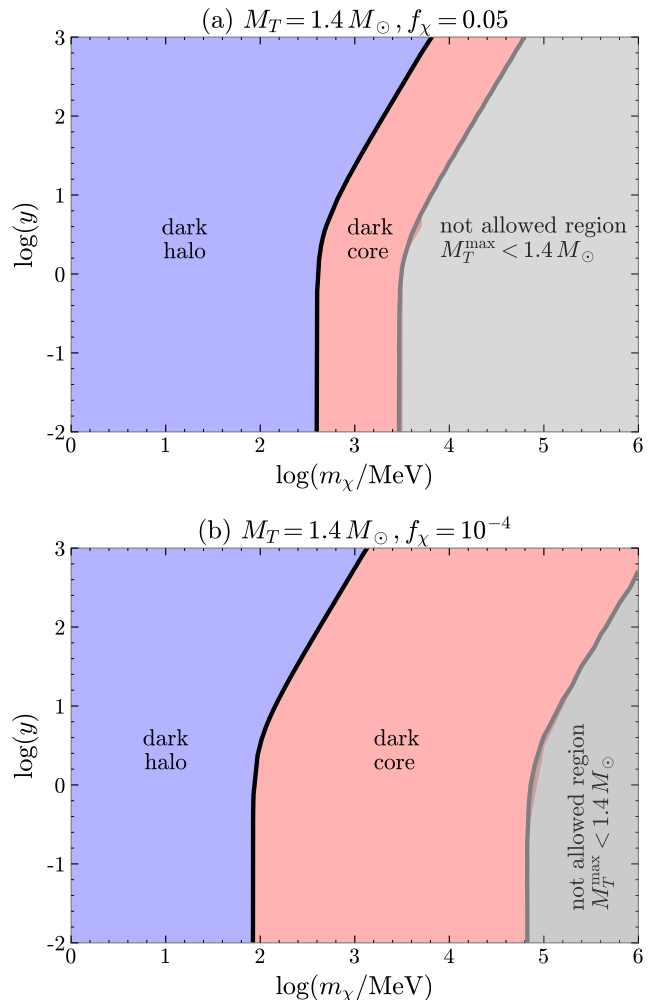


Figure 3. DM parameter space of a dark core/halo for a $M_T = 1.4 M_\odot$ DANs with (a) $f_\chi = 0.05$ (Ellis et al. 2018) (upper panel) and (b) $f_\chi = 10^{-4}$ (Nelson et al. 2019) (lower panel). The grey shaded regions in two panels correspond to $M_T^{\max} < 1.4 M_\odot$ and thus are not allowed.

In Fig. 3 we show the (m_χ, y) parameter spaces for DM particles forming a dark core/halo. The calculations are done with a fixed total gravitational mass $M_T = 1.4 M_\odot$. As expected, for both cases of DM fractions, light/heavy DM particles tend to form a dark halo/core, and large/small interaction strengths tend to create a dark halo/core. The solid black lines in Fig. 3 mark the borders of the purple dark-halo regions and the pink dark-core regions. At small interaction strengths, the solid black lines are almost parallel to the y axis, while at large interaction strengths, there is $m_\chi \propto y^{1/2}$. When decreasing the DM fraction from $f_\chi = 0.05$ (in the upper panel) to 10^{-4} (in the lower panel), the dark-halo (dark-core) region shrinks (expands), with the black border lines shifting slightly to the left.

For given DM properties, the critical DM fraction, f_χ^{crit} , can be calculated, at which the radii of the baryonic matter and DM components coincide, i.e., $R_B = R_D$. In Fig. 4, we report the critical DM fractions as functions of the DM particle mass (left panel) and the interaction strength (right panel). In the left panel, we see that there exists an excellent correlation between m_χ and f_χ^{crit} as $f_\chi^{\text{crit}} \propto m_\chi^4$. The right panel shows that $f_\chi^{\text{crit}} \simeq \text{const}$ for $y \ll 1$ but $f_\chi^{\text{crit}} \propto y^{-2}$ when $y \gg 1$. In the following, we further demonstrate and examine in detail the dependence of f_χ^{crit} on the DM properties.

We first raise a new criterion for the formation of a dark core/halo. We begin with the chemical potential in the proper frame, μ_c , which should be a constant throughout the equilibrium configuration (Kodama & Yamada 1972), i.e.,

$$\mu_c = \mu \sqrt{g(r)} = \text{const} , \quad (9)$$

where $\mu = d\epsilon/dn$ is the chemical potential in local Lorentz frame and $g(r)$ is the (t, t) component of the metric. By defining the relativistic specific enthalpy h as:

$$h = \int \frac{dP}{\epsilon + P} = \int \frac{d\mu}{\mu} , \quad (10)$$

we find the derivative ¹:

$$\frac{dh}{dr} = -\frac{d \ln \sqrt{g(r)}}{dr} , \quad (11)$$

is only a function of r . Therefore, the decreases of the enthalpies of two components, h_B and h_D , must be equal in the same radial interval $[r, r + dr]$. Combining with the fact that the decrease of h_B/h_D will terminate once h_B/h_D vanishes at the surface of baryonic matter/DM, we conclude that the formation of a dark core/halo is determined by the central enthalpies of the two components, i.e.,

$$\begin{aligned} h_D^c < h_B^c &\Rightarrow \text{dark core} , \\ h_D^c > h_B^c &\Rightarrow \text{dark halo} , \end{aligned}$$

where h_B^c and h_D^c are the central enthalpies of the baryon and DM components, respectively.

With this criterion at hand, we proceed to derive the critical DM fraction of a DANS. In such critical cases, we denote the central enthalpy as $h_c \equiv h_B^c = h_D^c$ and the radius $R \equiv R_B = R_D$. For fermionic DM considered in the present paper, we have:

$$h_c = \ln \left(\sqrt{1 + x^2} + \frac{2y^2}{3\pi^2} x^3 \right) . \quad (12)$$

¹ Another conclusion from this derivative is that the ratio of the two chemical potentials, μ_B/μ_D , is a constant throughout the stellar, see e.g. Goldman et al. (2013); Ivanytskyi et al. (2020).

Then the asymptotic solutions of x can be found analytically for small and large interaction strengths, i.e.,

$$x = \begin{cases} \sqrt{e^{2h_c} - 1} , & y \ll 1 , \\ \left(\frac{3\pi^2 \epsilon^{h_c}}{2y^2} \right)^{1/3} , & y \gg 1 . \end{cases} \quad (13)$$

For current observed NSs with $M \sim 1-2 M_\odot$, the central enthalpy is $h_c \sim 0.1-0.3$. Under such a range of h_c , the DM energy density ϵ_χ is dominated by the rest-mass term (see Appendix A for detailed discussions), i.e., $\epsilon_\chi \simeq m_\chi n_\chi = m_\chi^4 x^3 / (3\pi^2)$. Then the amount of DM could be estimated as $M_D \simeq \epsilon_\chi R^3 = x^3 m_\chi^4 R^3 / (3\pi^2)$, or equivalently,

$$f_\chi^{\text{crit}} \simeq 5 \times 10^{-7} \left(\frac{x}{0.1} \right)^3 \left(\frac{m_\chi}{100 \text{MeV}} \right)^4 \left(\frac{1.4 M_\odot}{M_T} \right) \left(\frac{R}{12 \text{km}} \right)^3 . \quad (14)$$

We here mention that Eq.(14) together with Eq.(13) can be used to explain all the features previously observed for f_χ^{crit} in Fig. 3 and Fig. 4:

- From Eq.(14), $m_\chi \propto x^{-3/4}$ at fixed f_χ^{crit} ; Then from Eq.(13), m_χ does not rely on the value of y if $y \ll 1$, whereas $m_\chi \propto y^{1/2}$ if $y \gg 1$, as shown in Fig. 3;
- Obviously from Eq.(14), $f_\chi \propto m_\chi^4$, as shown in Fig. 4 (in the left panel);
- Substituting x in Eq.(14) by Eq.(13), one can easily find that f_χ is independent of y for $y \ll 1$, while $f_\chi \propto y^{-2}$ for $y \gg 1$, as shown in Fig. 4 (in the right panel).

4. DARK-HALO EFFECTS ON THE PULSAR PULSE PROFILE

Based on the oblate Schwarzschild approximation for the NS spacetime (Morsink et al. 2007), the pulse-profile modeling technique has been used by the Neutron Star Interior Composition Explorer (NICER) [see Watts et al. (2016); Watts (2019) and references therein] to deliver tight constraints on the mass and radius of NSs (Riley et al. 2019, 2021; Miller et al. 2019, 2021) and to pin down the unknown dense matter EOS (Miller et al. 2019; Raaijmakers et al. 2019, 2021). Since the pulse profile may be modified due to the extra gravitational potential of the dark halo (Di Giovanni et al. 2022), in this section, we numerically calculate the pulse profiles of DANSs and investigate the effects resulting from the existence of a dark halo.

In this first attempt at studying the dark-halo effects on the pulse profiles, several simplifications are in order. We assume the radiation emitted from two point-like spots sitting oppositely on the baryon surface (i.e., at

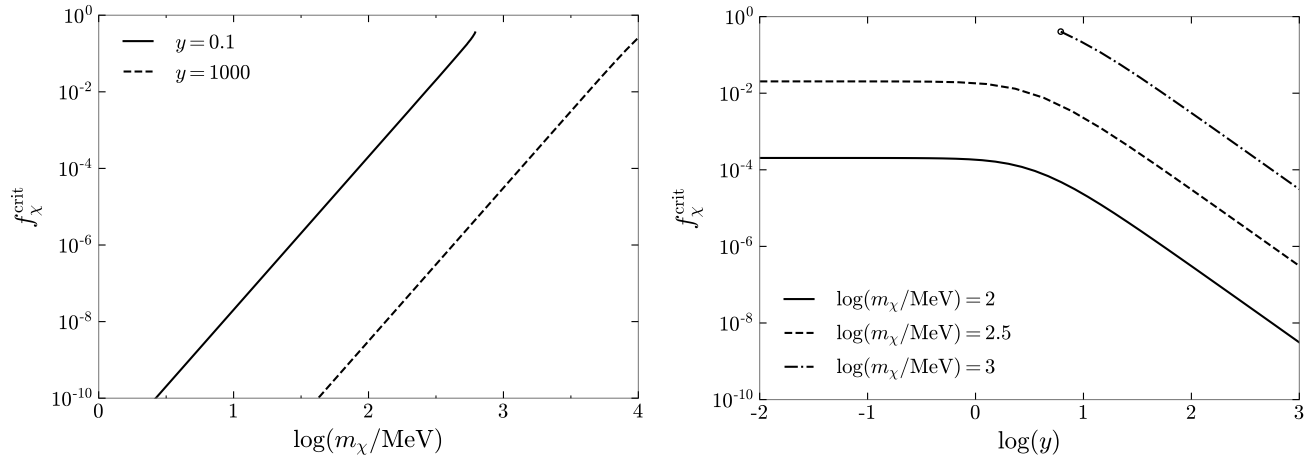


Figure 4. (Left panel) Critical DM fraction as a function of DM particle mass for different interaction strengths; (Right panel) Critical DM fraction as a function of the interaction strengths for different DM particle masses. For each panel the DANS mass is fixed at $M_T = 1.4 M_\odot$ and the baryon component is described by NL3 $\omega\rho$ EOS. The dash-dotted line in the right panel ends at the circular symbol, due to small values of the interaction strength could not support a $M_T = 1.4 M_\odot$ DANS.

Table 1. Properties of two constructed DANS models, by fixing $M_T(R_B) \equiv M_B(R_B) + M_D(R_B) = 1.4 M_\odot$ and $M_{\text{halo}} \equiv M_T - M_T(R_B) = 0.15 M_\odot$ but varying the DM particle mass m_χ and the interaction strength y . The corresponding pure NS cases, which share the same $M_T(R_B)$ and R_B with the two DANSSs, respectively, are also listed.

Model	m_χ/GeV	$\log(y)$	$M_T(R_B)/M_\odot$	M_{halo}/M_\odot	M_T/M_\odot	f_χ	R_B/km	R_D/km	M_{halo}/R_D
DANS I	0.1	1.5	1.4	0.15	1.55	0.096	13.75	2771.4	8.0×10^{-5}
pure NS I	–	–	1.4	0	1.4	0	13.75	–	0
DANS II	1	1.5	1.4	0.15	1.55	0.173	13.23	28.7	7.7×10^{-3}
pure NS II	–	–	1.4	0	1.4	0	13.23	–	0

$r = R_B$). And the specific intensity of the radiation is assumed to be isotropic (Miller & Lamb 1998). We do include the Doppler boost and relativistic aberration in our calculation but neglect the frame-dragging and the stellar deformation due to rotation. We also assume that the distance between the DANS and the observer is large enough to be treated mathematically as infinity. Below we introduce the necessary formalism for the calculations.

The observed differential flux at distance D from a point-like spot is given by (see e.g., Poutanen & Beloborodov 2006, for a detailed derivation):

$$dF = \delta^5 g(R_B) I'(\nu') d\nu' \cos \alpha \frac{d \cos \alpha}{d \cos \psi} \frac{dS'}{D^2}, \quad (15)$$

where δ is the Doppler factor. $I'(\nu')$ is the radiation intensity at the comoving frame. α is the emission angle and ψ is the angle between the local radial direction and the line of sight. dS' is the proper differential area where the photons are emitted (see Fig. 1 in Poutanen & Beloborodov (2006) for illustration).

For further analysis, we use the bolometric flux normalized by $\int I'(\nu') d\nu' dS'/D^2$,

$$F \equiv \frac{D^2 \int dF}{dS' \int I'(\nu') d\nu'} = \delta^5 g(R_B) \cos \alpha \frac{d \cos \alpha}{d \cos \psi}. \quad (16)$$

Here Eq.(16) accounts for the special relativistic effects (Doppler boost and relativistic aberration), the gravitational redshift and light bending.

To obtain the normalized flux, one need to determine the value of ψ and the relation between ψ and α . The later can be derived from the photon geodesic equation as (see Appendix B for derivation):

$$\psi = \int_{R_B}^{\infty} \frac{\sqrt{fg}}{r^2} \left[\frac{1}{b^2} - \frac{g}{r^2} \right]^{-1/2} dr, \quad (17)$$

where $b = R_B \sin \alpha / \sqrt{g(R_B)}$ is the impact parameter. $f(r)$ is the (r, r) component of the metric.

On the other hand, ψ can be obtained from the geometry relation:

$$\cos \psi = \cos i \cos \theta + \sin i \sin \theta \cos(2\pi \nu t), \quad (18)$$

where i is the inclination angle of the spin axis to the line of sight, θ is the spot colatitude and ν is the rotation frequency. Here $t = 0$ is chosen when the spot is closest to the observer.

With ψ at hand, we invert Eq. (17) to get α . Then we can calculate the Doppler factor δ and $d(\cos \alpha)/d(\cos \psi)$ and obtain the normalized flux. Finally, the time-delay effects caused by different traveling paths of the emitted photons should be considered (see Appendix B for derivation):

$$\Delta t = \int_{R_B}^{\infty} \sqrt{\frac{f}{g}} \left[\left(1 - \frac{b^2 g}{r^2} \right)^{-1} - 1 \right] dr. \quad (19)$$

We correct the observer time as $t_{\text{obs}} = t + \Delta t$.

For the following study, we define two new masses, namely, (i) $M_T(R_B) \equiv M_B(R_B) + M_D(R_B)$, which corresponds to the total gravitational mass inside the baryon radius R_B ; (ii) $M_{\text{halo}} \equiv M_T - M_T(R_B)$, which corresponds to the mass of the dark halo. It is obvious that $M_T(R_B) = M_T$ in the absence of a dark halo; otherwise, $M_T(R_B) < M_T$. Notice that the original Schwarzschild spacetime outside a pure NS with no halo would be altered when adding a dark halo. The change can be characterized by the increase of $g(R_D)$ as:

$$\Delta g(R_D) = \left(1 - \frac{2M_T(R_B)}{R_D} \right) - \left(1 - \frac{2M_T}{R_D} \right) = \frac{2M_{\text{halo}}}{R_D}. \quad (20)$$

Hereafter we choose M_{halo}/R_D as a characteristic parameter and will show that the modification of the pulse profile depends sensitively on M_{halo}/R_D .

In Table 1 we construct two DANSs by fixing $M_T(R_B) = 1.4 M_{\odot}$ and $M_{\text{halo}} = 0.15 M_{\odot}$ but varying the DM particle properties. Their corresponding pure NSs, which share the same $M_T(R_B)$ and R_B with them, respectively, are also listed. It should be emphasized that the values of M_{halo}/R_D are quite different for the two constructed DANSs. In Fig. 5, we plot the metric as a function of the radius. We note that the metric functions of the DANSs deviate from their corresponding pure NS ones. Meanwhile, the deviation close to the star can be characterized by M_{halo}/R_D since they are of the same order of magnitude.

In Fig. 6 we show the pulse profiles for the DANSs and pure NSs listed in Table 1. We take the spot colatitude $\theta = \pi/4$, the inclination angle $i = \pi/4$ and the rotating frequency $\nu = 200$ Hz in calculation. It is noticeable that the pulse profiles of DANSs deviate from the pure NS cases. The difference appears mainly in the amplitudes of the normalized flux, whereas the phase shift is almost negligible. The peak flux deviation is about 6% for model DANS II ($M_{\text{halo}}/R_D = 7.7 \times 10^{-3}$) but only

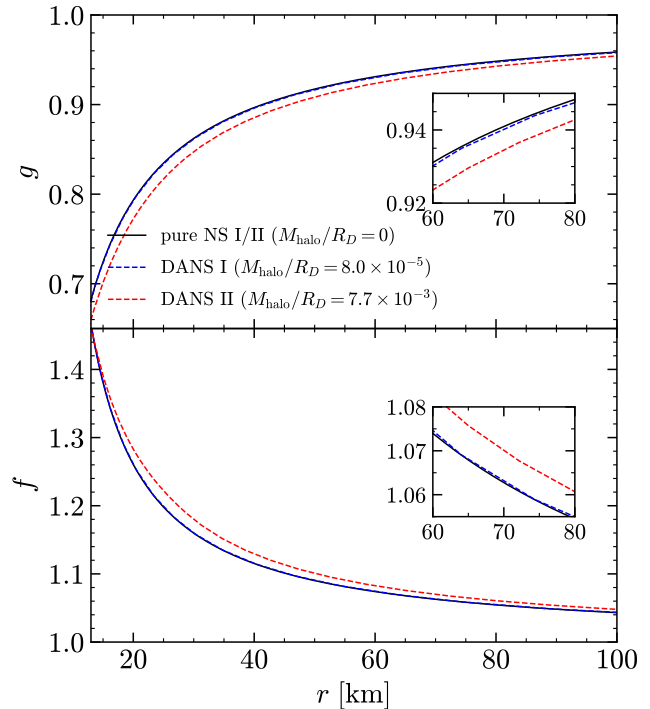


Figure 5. Metric components $g(r)$ and $f(r)$ as functions of the radius r for DANS models listed in Table 1. The Schwarzschild metrics outside a pure NS with $M_T = 1.4 M_{\odot}$, $g = 1 - 2M_T/r$ and $f = (1 - 2M_T/r)^{-1}$, is also shown with black solid curves.

0.05% for model DANS I ($M_{\text{halo}}/R_D = 8 \times 10^{-5}$). The nearly two orders of magnitude difference between the peak flux deviations is close to the difference between M_{halo}/R_D , implying that the peak flux deviation may strongly depend on M_{halo}/R_D .

To clarify this dependence, in Fig. 7, we show in detail the peak flux deviation as a function of M_{halo}/R_D for dozens of DANS models. These DANSs are generated with parameters chosen randomly throughout the parameter spaces of $\log(m_{\chi}/\text{MeV}) \in [0, 6]$, $\log(y) \in [-2, 3]$, $M_T \in [1, 2.5] M_{\odot}$, $f_{\chi} \in [0, 0.5]$, $i \in [\pi/6, \pi/2]$, $\theta \in [\pi/6, \pi/2]$ and $\nu \in [100, 400]$ Hz. We observe an approximate linear correlation between the peak flux deviation and M_{halo}/R_D in logarithmic space, i.e.,

$$\log \left(\frac{|\Delta F_{\text{peak}}|}{F_{\text{peak}}} \right) = 0.998 \log \left(\frac{M_{\text{halo}}}{R_D} \right) + 0.854. \quad (21)$$

with the corresponding coefficient of determination $R^2 = 0.995$. It is seen that for compact dark halos with $M_{\text{halo}}/R_D \simeq 0.01$, the deviations of peak flux can reach about 10%. Therefore it may be relevant for the NICER analysis of the mass and radius of X-ray pulsars for the study of dense matter EOS, and we also expect that such effects can be detected with future X-ray data. We mention here that, although our study provides a connection

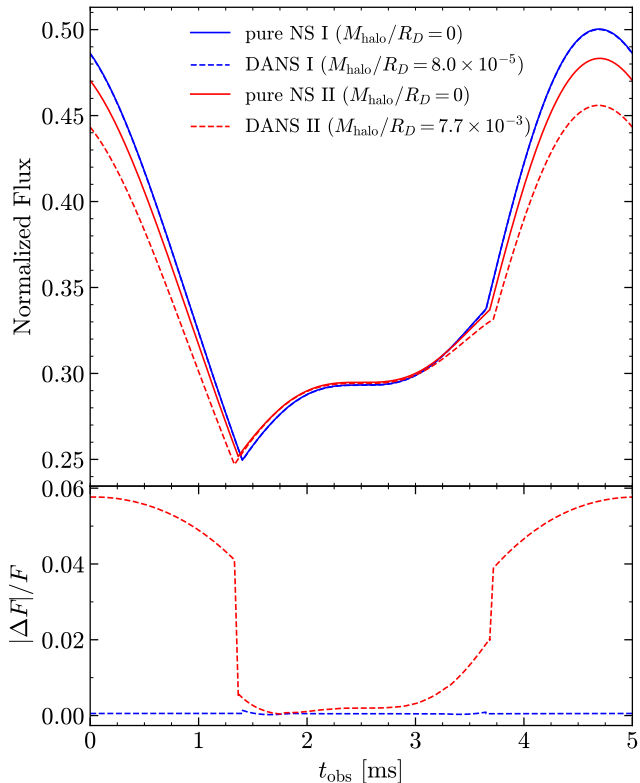


Figure 6. Pulse profiles from two point-like spots for the DANSs listed in Table 1 (dashed curves). The spot colatitude at northern hemisphere is $\theta = \pi/4$ and the inclination angle of the spin axis to the light of sight $i = \pi/4$. The rotating frequency is taken to be $\nu = 200$ Hz. The corresponding pure NS cases with same $M_T(R_B)$ and R_B are also shown (solid curves). Note the two pure NS cases are not the same, due to the small difference in the radii of the baryon component R_B (see Table 1).

of the observed flux with the microscopic physics of DM and baryonic matter, it is only a first, crude approximation to the phenomena occurring in the observed flux of X-ray pulsars, see discussions in, e.g., Lo et al. (2013); Psaltis et al. (2014); Miller & Lamb (2015). A more detailed analysis incorporating, e.g., the number of photon counts and the background emission, will be performed in the future for the observability related to DM halo.

5. DARK MATTER PARTICLE PROPERTIES

In this section, we perform Bayesian parameter estimation on the unknown DM parameters, using the available NICER mass-radius measurements of two X-ray pulsars, i.e., PSR J0030+0451 (Miller et al. 2019; Riley et al. 2019) and PSR J0740+6620 (Miller et al. 2021; Riley et al. 2021). As illustrated above (see Sec. 3.2), h_c plays an important role in determining the core/halo configuration. Therefore, it is convenient to combine the central enthalpy of baryonic matter h_B^c and the ratio of

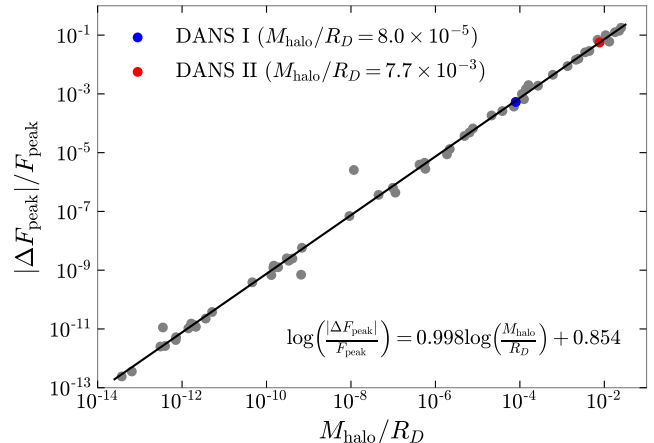


Figure 7. Peak flux deviation as a function of M_{halo}/R_D . The grey dots correspond to the results from dozens of DANS models, which are generated with parameters chosen randomly throughout a wide parameter space (see text for details). The blue and red dots are results from the two DANSs shown in Fig. 6, respectively. The empirical relation is shown with a solid black line.

the two enthalpies $q \equiv h_D^c/h_B^c$, as well as the DM parameters m_χ and y , into a vector θ . The total likelihood function in our analysis is expressed as:

$$p(\{M_i, R_i\}|\theta) = \prod_i p_i(M_{T,i}(R_B), R_{B,i}|\theta), \quad (22)$$

where we equate the individual likelihood p_i of observation i to the joint posterior distributions of M_i and R_i reported by NICER (Riley et al. 2019, 2021). Since the pulse-profile modeling of NICER should be modified for DANSs and one could not apply the NICER measurements to study DANSs directly. We simply treat $M_{T,i}(R_B)$ and $R_{B,i}$ as the measured mass and radius. Such treatment should be valid as long as M_{halo}/R_D is sufficiently small, and we consider two cases being consistent with it, i.e., (i) $M_{\text{halo}}/R_D \leq 10^{-3}$; thus, the corresponding flux deviations are smaller than $\sim 1\%$, and (ii) $M_{\text{halo}}/R_D = 0$, which is equivalent to a dark core scenario.

We take logarithmic uniform distributions for the DM particle mass ($\log(m_\chi/\text{MeV}) \sim U[0, 6]$) and for the interaction strength ($\log(y) \sim U[-2, 3]$). The priors of h_B^c are uniform distributed in the range of $[0.1, 0.5]$ and $[0.2, 0.6]$ for PSR J0030+0451 and PSR J0740+6620, respectively. We also set uniform distributions for both cases of $M_{\text{halo}}/R_D \leq 10^{-3}$ ($q \sim U[0, 3]$) and for the case of $M_{\text{halo}}/R_D = 0$ ($q \sim U[0, 1]$). Note that $q \leq 1$ corresponds to a dark core.

With the priors and the likelihood function at hand, we sample from the posterior density using the nested sampling software PYMULTINEST (Buchner et al. 2014).

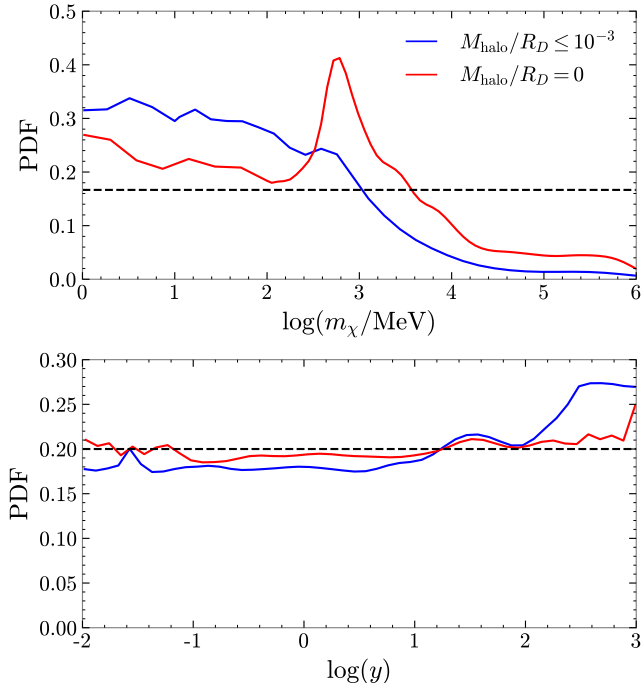


Figure 8. Posterior distributions of the DM particle mass (upper panel) and the interaction strength (lower panel). The corresponding priors are shown as black dashed lines.

The resulting probability density functions (PDFs) of the DM particle mass and of the interaction strength are shown in Fig. 8.

The obtained PDFs of the DM particle mass are quite different for the two cases. Assuming $M_{\text{halo}}/R_D \leq 10^{-3}$, the observational data prefers light DM particles and we can place a 90% upper limit of $m_\chi \leq 1.5$ GeV. Heavier particles are mostly excluded because they tend to reduce the maximum mass of DANS below the masses of PSR J0030+0451 or PSR J0740+6620. Whereas assuming $M_{\text{halo}}/R_D = 0$, there shows a prominent peak at $m_\chi \sim 0.6$ GeV. The peak can be understood by considering the requirement of a dark core: Light DM particles more easily form a dark halo and thus are more likely to be rejected in the nested sampling process. At the same time, to support the masses of observed pulsars, m_χ favors those values which are not too large. Nevertheless, the interaction strength y is poorly constrained by the observations of the pulsar pulse profile; due to that, within the current modeling of DM particles, the DM rest-mass term dominates the DM energy and pressure (see Appendix. A). Nevertheless, as mentioned above, since the interaction strength could affect the tidal deformability via affecting the radius of the DM component, future tidal deformability measure-

ments from gravitational waves hold the promise of providing a complementary constraint on the interaction strength.

6. SUMMARY AND CONCLUSIONS

In this paper, we study how DM, admixed with ordinary baryonic matter in different distributions, changes the structure and observations of NSs and confront the DANS properties with NS observational data. We consider DM as MeV-GeV self-interaction fermions and explore in detail the two possible scenarios, namely the dark halo and the dark core.

Although the formation of a dark core/halo depends complicatedly on the DM particle mass (m_χ) and self-interacting strength (y) as well as the fraction of DM accumulated (f_χ). We here show that these dependencies can be understood in a unified manner from a newly-proposed criterion for identifying the formation of a dark core or a dark halo. That is, the formation of a dark core/halo is essentially determined by the central enthalpies of the baryonic and dark components. We further provide a general formula for the critical amount of DM, f_χ^{crit} , which is well consistent with the numerical results of solving the two-fluid TOV equations. In particular, f_χ^{crit} correlates linearly with the fourth power of the DM particle mass, i.e., $f_\chi^{\text{crit}} \propto m_\chi^4$; Also, f_χ^{crit} is insensitive to y in the weak interacting case ($y \ll 1$), but proportional to y^{-2} in the strong interacting case ($y \gg 1$).

For the first time, we also estimate the dark-halo effects on NS pulse profiles, which are observed in NICER-like X-ray missions. Our analysis reveals that the effects depend sensitively on the value of M_{halo}/R_D , and the modification in the peak flux deviation can reach up to $\sim 10\%$ if the dark halo is dense enough with $M_{\text{halo}}/R_D \simeq 0.01$. Furthermore, we show that the existence of a dark halo could increase the maximum mass while a dense dark core could dramatically decrease it, which is in agreement with previous works.

In addition, we apply the available NICER data to the DANS study and present a Bayesian parameter estimation of DM properties. In the dark-core scenario ($M_{\text{halo}}/R_D = 0$), we find a peak PDF for the DM particle mass at $m_\chi \simeq 0.6$ GeV; While in the dark-halo scenario, there is a more loose upper limit of $m_\chi \leq 1.5$ GeV at 90% confidence level when assuming $M_{\text{halo}}/R_D \leq 10^{-3}$. No new constraint is found for the interaction strength between DM particles by analyzing the present pulse observations of PSR J0030+0451 and PSR J0740+6620 from NICER.

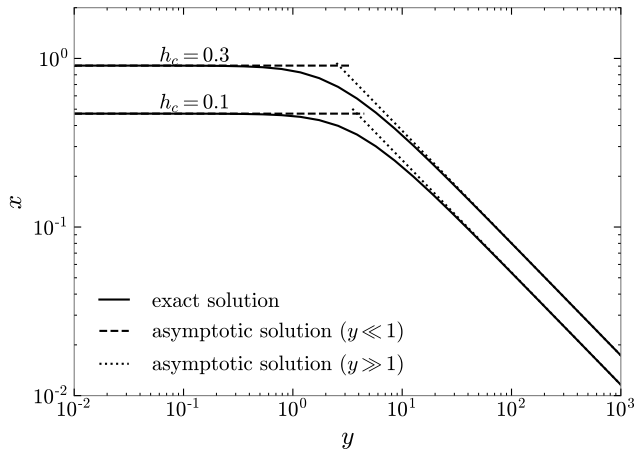


Figure 9. Dimensionless Fermi momentum x as a function of the interaction strength y for $h_c = 0.1$ and $h_c = 0.3$. Both the exact solutions of Eq. (12) and the asymptotic solutions of Eq.(13) are shown.

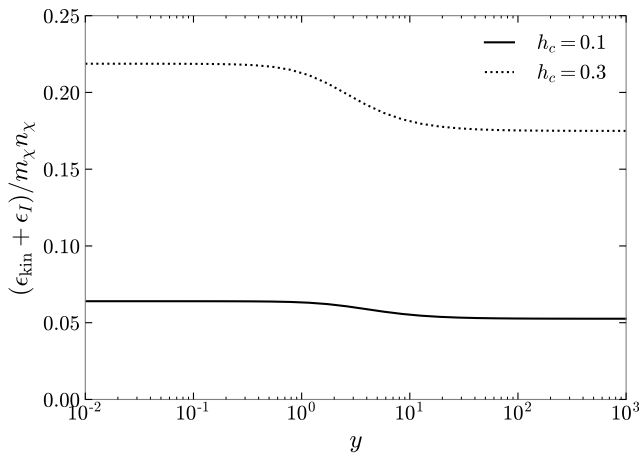


Figure 10. Kinetic and interaction energy density (scaled by the rest mass density) as a function of the interaction strength for $h_c = 0.1$ and $h_c = 0.3$.

A. THE DIMENSIONLESS FERMI MOMENTUM AND ENERGY DENSITY OF DARK MATTER

In Fig. 9, we report the exact solutions of the dimensionless Fermi momentum x from Eq. (12), together with the asymptotic solutions of Eq. (13). It is shown that the asymptotic solutions are sufficiently accurate for $y \lesssim 0.1$ or $y \gtrsim 10$. For the considered range of $h_c \simeq 0.1 - 0.3$ relevant to the present study, x always lies in the range from $\mathcal{O}(0.01)$ to $\mathcal{O}(0.1)$.

Substituting x into Eq.(3), we can calculate the energy density of DM. In Fig. 10 we plot the kinetic and interaction energy density as a function of the interaction strength. We find that in the considered range of h_c , the kinetic and interaction energy density would not exceed $\sim 20\%$ of the rest-mass density. This justifies the approximation $\epsilon_\chi \simeq m_\chi n_\chi$ we use in the context.

B. LIGHT BENDING AND TIME DELAY

Since we neglect the rotation effect on the spacetime, the metric is spherically symmetric and can be written as

$$ds^2 = -g(r)dt^2 + f(r)dr^2 + r^2 d\theta^2 + r^2 \sin^2 \theta d\phi^2 . \quad (\text{B1})$$

The spherical symmetry allows us to confine the photon geodesic to the equatorial plane (i.e., $\theta = \pi/2$). Then one can choose an affine parameter λ such that

$$\frac{dt}{d\lambda} = \frac{1}{g}, \quad (\text{B2})$$

$$\frac{dr}{d\lambda} = f^{-1/2} \left(\frac{1}{g} - \frac{b^2}{r^2} \right)^{1/2}, \quad (\text{B3})$$

$$\frac{d\theta}{d\lambda} = 0, \quad (\text{B4})$$

$$\frac{d\phi}{d\lambda} = \frac{b}{r^2}, \quad (\text{B5})$$

where b is the impact parameter. The impact parameter is related to the emission angle at the baryon surface as $b = R_B \sin \alpha / \sqrt{g(R_B)}$, which can be derived from the geometry $\tan \alpha = (U^\phi U_\phi)^{1/2} / (U^r U_r)^{1/2}$ (Beloborodov 2002).

Combining Eq.(B3) and Eq.(B5), we find

$$\frac{d\phi}{dr} = \frac{b}{r^2} \left(\frac{fg}{1 - b^2g/r^2} \right)^{1/2}, \quad (\text{B6})$$

Finally, by integrating Eq.(B6) from R_B to infinity, we obtain the angle between local radial direction and the line of sight as

$$\psi = \int_{R_B}^{\infty} \frac{d\phi}{dr} dr = \int_{R_B}^{\infty} \frac{\sqrt{fg}}{r^2} \left(\frac{1}{b^2} - \frac{g}{r^2} \right)^{-1/2} dr. \quad (\text{B7})$$

We now turn to calculate the time delay, which is caused by different travel paths of the emitted photons. The time delay can be calculated by combining Eq.(B2) and Eq.(B3),

$$t = \int_{R_B}^{\infty} \frac{dt}{dr} dr = \int_{R_B}^{\infty} \left(\frac{f}{g} \right)^{1/2} \left(1 - \frac{b^2g}{r^2} \right)^{-1/2} dr. \quad (\text{B8})$$

However, this integral diverges as $r \rightarrow \infty$. To avoid divergence, we define a relative time delay as (Pechenick et al. 1983; Poutanen & Beloborodov 2006):

$$\Delta t = t(b) - t(0) = \int_{R_B}^{\infty} \left(\frac{f}{g} \right)^{1/2} \left[\left(1 - \frac{b^2g}{r^2} \right)^{-1/2} - 1 \right] dr. \quad (\text{B9})$$

which is defined with respect to a photon emitted from the spot closest to the observer. As a result, the observer time should be corrected as $t_{\text{obs}} = t + \Delta t$.

ACKNOWLEDGEMENTS

We are thankful to W.-Z. Jiang, B. Qi, Q.-F. Xiang and the XMU neutron star group for helpful discussions. The work is supported by National SKA Program of China (No. 2020SKA0120300), the National Natural Science Foundation of China (Grant No. 11873040), the science research grants from the China Manned Space Project (No. CMS-CSST-2021-B11), and the Youth Innovation Fund of Xiamen (No. 3502Z20206061).

Software: PyMultiNest (Buchner et al. 2014, <https://github.com/JohannesBuchner/PyMultiNest>).

REFERENCES

- Abbott, B. P., Abbott, R., Abbott, T. D., et al. 2017, *PhRvL*, 119, 161101. doi:10.1103/PhysRevLett.119.161101
- Abbott, R., Abbott, T. D., Abraham, S., et al. 2020, *ApJL*, 896, L44. doi:10.3847/2041-8213/ab960f
- Bauswein, A., Guo, G., Lien, -H., et al. 2020, arXiv:2012.11908
- Beloborodov, A. M. 2002, *ApJL*, 566, L85. doi:10.1086/339511

- Bertone, G. & Fairbairn, M. 2008, *PhRvD*, 77, 043515.
doi:10.1103/PhysRevD.77.043515
- Bezares, M., Viganò, D., & Palenzuela, C. 2019, *PhRvD*, 100, 044049. doi:10.1103/PhysRevD.100.044049
- Buchner, J., Georgakakis, A., Nandra, K., et al. 2014, *A&A*, 564, A125. doi:10.1051/0004-6361/201322971
- Ciarcelluti, P. & Sandin, F. 2011, *Physics Letters B*, 695, 19. doi:10.1016/j.physletb.2010.11.021
- Das, A., Malik, T., & Nayak, A. C. 2019, *PhRvD*, 99, 043016. doi:10.1103/PhysRevD.99.043016
- Das, H. C., Kumar, A., Kumar, B., et al. 2020, *MNRAS*, 495, 4893. doi:10.1093/mnras/staa1435
- Das, H. C., Kumar, A., & Patra, S. K. 2021, *PhRvD*, 104, 063028. doi:10.1103/PhysRevD.104.063028
- de Lavallaz, A. & Fairbairn, M. 2010, *PhRvD*, 81, 123521. doi:10.1103/PhysRevD.81.123521
- Dengler, Y., Schaffner-Bielich, J., & Tolos, L. 2022, *PhRvD*, 105, 043013. doi:10.1103/PhysRevD.105.043013
- Di Giovanni, F., Sanchis-Gual, N., Cerdá-Durán, P., et al. 2022, *PhRvD*, 105, 063005. doi:10.1103/PhysRevD.105.063005
- Ellis, J., Hütsi, G., Kannike, K., et al. 2018, *PhRvD*, 97, 123007. doi:10.1103/PhysRevD.97.123007
- Fan, Y.-Z., Yang, R.-Z., & Chang, J. 2011, *PhRvD*, 84, 103510. doi:10.1103/PhysRevD.84.103510
- Fasano, M., Wong, K. W. K., Maselli, A., et al. 2020, *PhRvD*, 102, 023025. doi:10.1103/PhysRevD.102.023025
- Goldman, I., Mohapatra, R. N., Nussinov, S., et al. 2013, *Physics Letters B*, 725, 200. doi:10.1016/j.physletb.2013.07.017
- Goldman, I. & Nussinov, S. 1989, *PhRvD*, 40, 3221. doi:10.1103/PhysRevD.40.3221
- Gonzalez, D. & Reisenegger, A. 2010, *A&A*, 522, A16. doi:10.1051/0004-6361/201015084
- Gresham, M. I. & Zurek, K. M. 2019, *PhRvD*, 99, 083008. doi:10.1103/PhysRevD.99.083008
- Horowitz, C. J. & Piekarewicz, J. 2001, *PhRvL*, 86, 5647. doi:10.1103/PhysRevLett.86.5647
- Husain, W. & Thomas, A. W. 2021, *JCAP*, 2021, 086. doi:10.1088/1475-7516/2021/10/086
- Ivanytskyi, O., Sagun, V., & Lopes, I. 2020, *PhRvD*, 102, 063028. doi:10.1103/PhysRevD.102.063028
- Kain, B. 2021, *PhRvD*, 103, 043009. doi:10.1103/PhysRevD.103.043009
- Kodama, T. & Yamada, M. 1972, *Progress of Theoretical Physics*, 47, 444. doi:10.1143/PTP.47.444
- Kopp, J., Laha, R., Opferkuch, T., et al. 2018, *Journal of High Energy Physics*, 2018, 96. doi:10.1007/JHEP11(2018)096
- Kouvaris, C. 2008, *PhRvD*, 77, 023006. doi:10.1103/PhysRevD.77.023006
- Kouvaris, C. & Tinyakov, P. 2010, *PhRvD*, 82, 063531. doi:10.1103/PhysRevD.82.063531
- Kouvaris, C. & Nielsen, N. G. 2015, *PhRvD*, 92, 063526. doi:10.1103/PhysRevD.92.063526
- Lee, B. K. K., Chu, M.-. chung ., & Lin, L.-M. 2021, *ApJ*, 922, 242. doi:10.3847/1538-4357/ac2735
- Leung, S.-C., Chu, M.-C., & Lin, L.-M. 2011, *PhRvD*, 84, 107301. doi:10.1103/PhysRevD.84.107301
- Leung, S.-C., Chu, M.-C., & Lin, L.-M. 2012, *PhRvD*, 85, 103528. doi:10.1103/PhysRevD.85.103528
- Li, A., Liu, T., Gubler, P., et al. 2015, *Astroparticle Physics*, 62, 115. doi:10.1016/j.astropartphys.2014.08.001
- Li, A., Huang, F., & Xu, R.-X. 2012, *Astroparticle Physics*, 37, 70. doi:10.1016/j.astropartphys.2012.07.006
- Li, X. Y., Wang, F. Y., & Cheng, K. S. 2012, *JCAP*, 2012, 031. doi:10.1088/1475-7516/2012/10/031
- Lo, K. H., Miller, M. C., Bhattacharyya, S., et al. 2013, *ApJ*, 776, 19. doi:10.1088/0004-637X/776/1/19
- Marrodán Undagoitia, T. & Rauch, L. 2016, *Journal of Physics G Nuclear Physics*, 43, 013001. doi:10.1088/0954-3899/43/1/013001
- Miller, M. C. & Lamb, F. K. 2015, *ApJ*, 808, 31. doi:10.1088/0004-637X/808/1/31
- Miller, M. C., Lamb, F. K., Dittmann, A. J., et al. 2019, *ApJL*, 887, L24. doi:10.3847/2041-8213/ab50c5
- Miller, M. C., Lamb, F. K., Dittmann, A. J., et al. 2021, *ApJL*, 918, L28. doi:10.3847/2041-8213/ac089b
- Miller, M. C. & Lamb, F. K. 1998, *ApJL*, 499, L37. doi:10.1086/311335
- Morsink, S. M., Leahy, D. A., Cadeau, C., et al. 2007, *ApJ*, 663, 1244. doi:10.1086/518648
- Motta, T. F., Guichon, P. A. M., & Thomas, A. W. 2018, *Journal of Physics G Nuclear Physics*, 45, 05LT01. doi:10.1088/1361-6471/aab689
- Mukhopadhyay, S., Atta, D., Imam, K., et al. 2017, *European Physical Journal C*, 77, 440. doi:10.1140/epjc/s10052-017-5006-3
- Narain, G., Schaffner-Bielich, J., & Mishustin, I. N. 2006, *PhRvD*, 74, 063003. doi:10.1103/PhysRevD.74.063003
- Nelson, A. E., Reddy, S., & Zhou, D. 2019, *JCAP*, 2019, 012. doi:10.1088/1475-7516/2019/07/012
- Panotopoulos, G. & Lopes, I. 2017, *PhRvD*, 96, 083004. doi:10.1103/PhysRevD.96.083004
- Pechenick, K. R., Ftaclas, C., & Cohen, J. M. 1983, *ApJ*, 274, 846. doi:10.1086/161498
- Pérez-García, M. Á. & Silk, J. 2012, *Physics Letters B*, 711, 6. doi:10.1016/j.physletb.2012.03.065

- Poutanen, J. & Beloborodov, A. M. 2006, MNRAS, 373, 836. doi:10.1111/j.1365-2966.2006.11088.x
- Psaltis, D., Özel, F., & Chakrabarty, D. 2014, ApJ, 787, 136. doi:10.1088/0004-637X/787/2/136
- Quddus, A., Panotopoulos, G., Kumar, B., et al. 2020, Journal of Physics G Nuclear Physics, 47, 095202. doi:10.1088/1361-6471/ab9d36
- Raaijmakers, G., Greif, S. K., Hebeler, K., et al. 2021, ApJL, 918, L29. doi:10.3847/2041-8213/ac089a
- Raaijmakers, G., Riley, T. E., Watts, A. L., et al. 2019, ApJL, 887, L22. doi:10.3847/2041-8213/ab451a
- Rafiei Karkevandi, D., Shakeri, S., Sagun, V., et al. 2022, PhRvD, 105, 023001. doi:10.1103/PhysRevD.105.023001
- Rezaei, Z. 2017, ApJ, 835, 33. doi:10.1088/1361-6528/aa5273
- Riley, T. E., Watts, A. L., Bogdanov, S., et al. 2019, ApJL, 887, L21. doi:10.3847/2041-8213/ab481c
- Riley, T. E., Watts, A. L., Ray, P. S., et al. 2021, ApJL, 918, L27. doi:10.3847/2041-8213/ac0a81
- Rrapaj, E. & Reddy, S. 2016, PhRvC, 94, 045805. doi:10.1103/PhysRevC.94.045805
- Sagun, V., Giangrandi, E., Ivanytskyi, O., et al. 2021, arXiv:2111.13289
- Sandin, F. & Ciarcelluti, P. 2009, Astroparticle Physics, 32, 278. doi:10.1016/j.astropartphys.2009.09.005
- Sen, D. & Guha, A. 2021, MNRAS, 504, 3354. doi:10.1093/mnras/stab1056
- Wang, X. D., Qi, B., Yang, G. L., et al. 2019, International Journal of Modern Physics D, 28, 1950148. doi:10.1142/S0218271819501487
- Watts, A. L. 2019, Xiamen-CUSTIPEN Workshop on the Equation of State of Dense Neutron-Rich Matter in the Era of Gravitational Wave Astronomy, 2127, 020008. doi:10.1063/1.5117798
- Watts, A. L., Andersson, N., Chakrabarty, D., et al. 2016, Reviews of Modern Physics, 88, 021001. doi:10.1103/RevModPhys.88.021001
- Wystub, S., Dengler, Y., Christian, J.-E., et al. 2021, arXiv:2110.12972
- Xiang, Q.-F., Jiang, W.-Z., Zhang, D.-R., et al. 2014, PhRvC, 89, 025803. doi:10.1103/PhysRevC.89.025803
- Zurek, K. M. 2014, PhR, 537, 91. doi:10.1016/j.physrep.2013.12.001